Int J Ind Chem (2017) 8:297–313
DOI 10.1007/s40090-016-0108-6

RESEARCH

Photocatalytic degradation of tetracycline aqueous solutions by nanospherical α-Fe_2O_3 supported on 12-tungstosilicic acid as catalyst: using full factorial experimental design

Majid Saghi[1] · **Kazem Mahanpoor**[1]

Received: 21 June 2016 / Accepted: 7 November 2016 / Published online: 16 November 2016

Abstract In this paper, spherical α-Fe_2O_3 nanoparticles (NPs) were supported on the surface of 12-tungstosilicic acid (12-TSA·$7H_2O$) using two different solid-state dispersion (SSD) and forced hydrolysis and reflux condensation (FHRC) methods. Photocatalytic activity of supported α-Fe_2O_3 NPs (α-Fe_2O_3/12-TSA·$7H_2O$) for tetracycline (TC) degradation in aqueous solution was investigated using UV/H_2O_2 process and the results were compared with that of pure α-Fe_2O_3 NPs. α-Fe_2O_3 and 12-TSA·$7H_2O$ were synthesized according to previous reports and all products were characterized by using FTIR, SEM, EDX and XRD. Design of experiments (DoEs) was utilized and photocatalytic degradation process was optimized using full factorial design. The experiments were designed considering four variables including pH, the initial concentration of TC, catalyst concentration and H_2O_2 concentration at three levels. TC concentration reduction in the medium was measured using UV/Vis spectroscopy at $\lambda_{max} = 357$ nm. The results of experiments indicated that supporting α-Fe_2O_3 NPs on the surface of 12-TSA·$7H_2O$ through SSD and FHRC methods caused to improve the filtration, recovery and photocatalytic activity of NPs. Also, it was indicated that those NPs supported through SSD method, have better photocatalytic performance than those supported through FHRC method. The statistical analyses revealed that the maximum TC degradation (97.39%) is obtained under those conditions in which pH and catalyst concentration variables are at maximum levels and the initial concentration of TC and H_2O_2 concentration variables are at minimum levels (pH 8, catalyst concentration = 150 ppm, initial concentration of TC = 30 ppm, H_2O_2 concentration = 0.1 ppm). A first order reaction with $k = 0.0098$ min^{-1} was observed for the photocatalytic degradation reaction.

Keywords Photocatalytic degradation · Tetracycline · α-Fe_2O_3 · 12-Tungstosilicic acid · α-Keggin

✉ Kazem Mahanpoor
k-mahanpoor@iau-arak.ac.ir

Majid Saghi
m-saghi@iau-arak.ac.ir

[1] Department of Chemistry, Islamic Azad University, Arak Branch, Arāk, Iran

Introduction

From the perspective of green chemistry, degradation of chemical pollutants in wastewater has attracted a lot of attention. Antibiotics are one of the larger groups of these pollutants in wastewater released from pharmaceutical industries [1]. Besides, TC is one broad spectrum of antibiotics repeatedly detected in urban and industrial wastewaters, drinking water, surface water and groundwater [2–6]. The molecular structure of TC is shown in Fig. 1. Various techniques are used to degrade TC; one of these techniques is photocatalytic degradation [7]. NPs play an important role in heterogeneous photocatalysis. Metal oxide NPs, i.e., iron oxides, have a special position in the science and technologies because of having wide applications and unique properties [8]. α-Fe_2O_3 (hematite) which is the most common form of iron oxides, has the rhombohedral structure and it is an attractive compound because of its applications in data storage, gas sensor, magnets materials, pigment, catalysis and photocatalysis [9–14]. Various techniques including co-precipitation, sol–gel, thermal decomposition, Micelle synthesis, sonochemical synthesis, hydrothermal synthesis and FHRC have

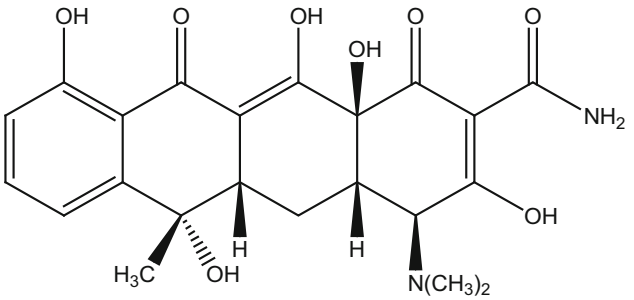

Fig. 1 Molecular structure of TC

been utilized to synthesize monodisperse α-Fe_2O_3 NPs. [15–21]. Among various photocatalytic processes, water and wastewater treatments are of the most important α-Fe_2O_3 NPs applications. In these processes, α-Fe_2O_3 NPs could be used in the form of a fine powder or crystals dispersed in water, but it is vital to know that filtering these NPs following reaction is difficult and costly. To solve this problem, researchers have examined methods for supporting α-Fe_2O_3 NPs on the surface of organic, inorganic or organic/inorganic catalyst supports [22, 23]. Various methods have been applied for supporting α-Fe_2O_3 NPs on the surface of catalyst support. Utilizing any of these methods depends on the chemical and physical properties of catalyst and catalyst support as well as the purpose of the process. One of these methods is SSD method in which catalyst precursor and catalyst support are separately synthesized and then are mixed with specific weight ratio using an appropriate solvent [24]. Then, during calcination, the catalyst is both formed and thermally supported on the surface of catalyst support. In another technique such as FHRC, the catalyst support is added to the precursor solution(s) during catalyst preparation (if it was stable in reaction medium) and the catalyst is supported on the surface of catalyst support while it is simultaneously formed. In FHRC method, all steps related to the synthesis of NPs were done on the surface of catalyst support and "NP/catalyst support" was obtained after nucleation and growth of NPs. Polyoxometalates (POMs) are a great class of inorganic compounds as multi-core metal–oxygen clusters [25]. If an atom named heteroatom (such as Si, P, As, B, etc.) enters the molecular structure of POM in addition to metal and oxygen, then heteropoly acids (HPAs) will be obtained [26]. Thermodynamically, HPAs have stable arrangements and maintain their crystal structure in aqueous and non-aqueous solutions. This class of materials has various applications in catalysis [27], analytical chemistry [28], medicinal chemistry (anti-tumor, anti-cancer, anti-bacteria, anti-microbial and anti-clotting) [29–31], radioactive materials [32] and gas absorbents [33] owing to their structural diversity and unique properties. HPAs have different crystal structures of which α-, β-, γ-, δ- and ε-Keggin, Wells–Dawson, Preysler, Stromberg and Anderson–Evans are served as critical types. 12-tungstosilicic acid (hereafter, 12-TSA) is a HPA with formula $H_4SiW_{12}O_{40}$ and α-Keggin crystal structure (see Fig. 2). The central Si heteroatom is surrounded by a tetrahedron whose oxygen vertices are each linked to one of the four W_3O_{13} sets. Each W_3O_{13} set consists of three W_3O_6 octahedrals linked in a triangular arrangement by sharing edges and the four W_3O_{13} are linked together by sharing corners [34]. So far, numerous experimental studies have been done about supporting HPAs on the surface of various organic and inorganic catalyst supports, but HPAs have rarely been used as catalyst support [35–38].

12-TSA has suitable physical and chemical properties to be used as a catalyst support. The pores existed on the crystalline surface of 12-TSA provide a suitable condition to support NPs [39]. To optimize a process like the photocatalytic degradation process, it is essential to study all factors influencing the process. But studying the effects of individual factors on the process is difficult and time-consuming, especially if these factors are not independent and they affect each other. Employing experimental design could eliminate these problems because the interaction effects of different factors could be attained using DoEs only. Full factorial is an appropriate method for DoEs because it could reduce the total number of experiments as well as optimize the process by optimizing all the affecting factors collectively, at a time [40]. The design could determine the effect of each factor on the response as well as how this effect varies with the change in level of other factors.

Various crystal structures of α-Fe_2O_3 NPs including rod-shape [21], spherical and elliptical forms [41] have been synthesized and identified until now. In this work, spherical α-Fe_2O_3 NPs are supported through two different SSD and FHRC methods on the surface of 12-TSA·$7H_2O$ (α-Fe_2O_3/12-TSA·$7H_2O$). Then, the performance of pure and supported α-Fe_2O_3 NPs on the TC photocatalytic degradation was investigated using full factorial experimental design.

Experimental

Material and apparatuses

All chemicals used in this work including sodium tungstate dihydrate, sodium silicate, diethyl ether, iron (III) chloride hexahydrate, urea, hydrogen peroxide (30% pure), hydrochloric acid (37% pure), sulfuric acid (96% pure), sodium hydroxide and ethanol were purchased from Merck and were used without further purification. The required TC was purchased from Razak pharmaceutical laboratory (Tehran, Iran). Also, deionized water was used throughout

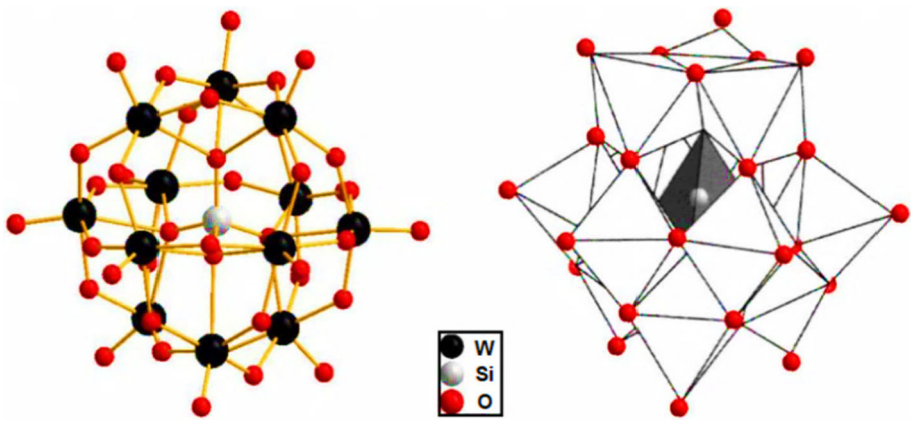

Fig. 2 α-Keggin structure of $[SiW_{12}O_{40}]^{4-}$

the experiments. The Fourier transform infra-red (FTIR) spectra of products were recorded on a Perkin-Elmer spectrophotometer (Spectrum Two, model) in the range of 450–4000 cm^{-1}. The shape, size and surface morphology of the synthesized 12-TSA·$7H_2O$ and α-Fe_2O_3/12-TSA·$7H_2O$ were examined using the obtained images of a Philips XL-30 scanning electron microscope (SEM). The X-ray diffraction (XRD) analysis of the samples was done using a DX27-mini diffractometer. BET surface area of materials was determined by N_2 adsorption–desorption method at 77 K, measured using a BELSORP-mini II instrument. The samples were degassed under vacuum at 473 K for 12 h before the BET measurement. All ultraviolet/visible (UV/Vis) absorption spectra were obtained using an Agilent 8453 spectrophotometer and the pH values were determined by a Metrohm pH meter model 827. Likewise, to separate the catalyst from samples, an ALC 4232 centrifuge was employed.

Synthesis of α-Fe_2O_3 NPs

The synthesis of α-Fe_2O_3 NPs was carried out according to Bharathi et al. [21]. Firstly, 100 ml iron (III) chloride hexahydrate 0.25 M which was considered as a source of Fe^{3+}, was poured into a flat-bottom flask. When Iron solution was agitated by stirrer, it was added drop by drop to it 100 ml urea 1 M (as a supplying agent of hydroxyl ions). The more gentle and regular adding urea, the smaller and more uniform-sized formed α-Fe_2O_3 particles will be. The obtained mixture was stirred for 30 min and then placed under the reflex at 90–95 °C for 12 h. Then, the precipitate after separation was washed with 100 ml deionized water because unreacted ions will be completely removed. The washed precipitate was dried at 70 °C for 2 h. Having fully dried, one light brown solid (iron hydroxide) was yielded. Finally, this solid remained at 300 °C for 1 h; hence the iron hydroxide particles will transform to iron oxide. Consequently, a dark brown solid of α-Fe_2O_3 was obtained.

Synthesis of 12-TSA·$7H_2O$

12-TSA·$7H_2O$ was synthesized according to literature procedure [42]. Firstly, 15 g sodium tungstate dihydrate was dissolved in 30 ml deionized water and then 1.16 g sodium silicate solution (density 1.375 g/ml) was added to it. The resulted mixture was heated up to about boiling point, and while it was stirred, 10 ml concentrated HCl was added to it during 30 min, smoothly. Then, the solution was naturally cooled down to RT and slight precipitate formed (silicic acid) in it was filtered. Again, 5 ml concentrated HCl was added to the solution and was transferred to separatory funnel after cooling it again down to RT. Then, 12 ml diethyl ether was added to it and well shaken. Therefore, three layers were formed inside separatory funnel, middle layer of which was yellow-colored. Bottom layer which was oily ether was separated and transferred into a beaker. To further extract, separatory funnel was further shaken again and the bottom layer was once more separated and transferred into the beaker. This extraction process was done so much that the yellow color of middle layer was fully faded. The extracted ether complex which was inside the beaker was transferred to another separatory funnel and then 16 ml HCl 25% (v/v) was added to it. Next, 4 ml diethyl ether was added to it, subsequently. The contents inside separatory funnel were shaken and bottom layer (ether) was transferred to the evaporating dish after separating. Evaporating dish was exposed to air and remained motionless to evaporate the solvent and form the 12-TSA·$7H_2O$ crystals. Finally, 12-TSA·$7H_2O$ formed crystals were placed at 70 °C for 2 h until it was completely dried. The chemical reaction occurred in the process of 12-TSA·$7H_2O$ synthesis has been shown in (1) [42].

$$12\ Na_2WO_4 + Na_2SiO_3 + 26\ HCl \rightleftarrows H_4SiW_{12}O_{40} \cdot xH_2O + 26\ NaCl + 11\ H_2O \quad (1)$$

Preparation of α-Fe_2O_3/12-TSA·7H_2O

SSD method

Firstly, the synthesized iron hydroxide (light brown solid) and 12-TSA·7H_2O catalyst support were mixed with weight ratio of 1:3 iron hydroxide/12-TSA·7H_2O (weight of catalyst support is three times of catalyst weight) using an agate pestle and mortar for 1 h. To have better mixture, ethanol was sprayed on the mixture until it becomes dough-form. During mixing, in the vaporization phase, ethanol is again added in order to keep the dough-form of the mixture. The resulted mixture was dried under air for 1 h and then was kept at 80 °C for 2 h. To do calcination and transform iron hydroxide particles fixed on the surface of 12-TSA·7H_2O into iron oxide (α-Fe_2O_3), the obtained solid was kept at 300 °C for 1 h.

FHRC method

Firstly, 50 ml iron (III) chloride hexahydrate 0.25 M was poured into a beaker. While it was agitated by stirrer, 3.5 g 12-TSA·7H_2O was gently added to it. The obtained mixture was stirred for 4–5 h. Then, stirring was stopped for 2 h until the solid within mixture was deposited. The solid accumulated at bottom of beaker was separated and transferred into one flat-bottom flask and the same 10 ml solution inside beaker was added to it. When mixture inside flat-bottom flask was being stirred, 50 ml urea 1 M was gradually added to it. The mixture was placed under reflux at 90–95 °C for 12 h. Then, the precipitate resulted after separation was washed with 100 ml ethanol/deionized water 1:1 solution because unreacted ions were completely removed. The washed precipitate was dried in the air for 2 h and then was kept at 80 °C for 2 h. In order to calcination, the obtained solid was kept at 300 °C for 1 h.

Full factorial experimental design

The photocatalytic efficiency of pure α-Fe_2O_3 NPs and α-Fe_2O_3/12-TSA·7H_2O prepared by SSD and FHRC methods on the TC degradation were investigated using DoE. The experiments were designed considering four variables including pH, the initial concentration of TC, catalyst concentration and H_2O_2 concentration at three levels. Experimental range and levels of variables are shown in Table 1. pH varied from 4 to 8 at three levels (4, 6 and 8), the initial concentration of TC from 30 to 70 ppm at three levels (30, 50 and 70 ppm), catalyst concentration from 50 to 150 ppm at three levels (50, 100 and 150 ppm) and H_2O_2 concentration from 0.1 to 0.5 ppm at three levels (0.1, 0.3 and 0.5 ppm). In Table 2, 19 experiments related to this factorial design and their experimental conditions have been listed. The removal efficiency of TC was a dependent response. In order to do DoEs, Minitab 16 version 16.2.0 statistical software was utilized. Also, analysis of variance (ANOVA) was run to analyze the results.

Table 1 Experimental range and levels of the variables

Variables	Range and levels		
	−1	0	+1
pH	4	6	8
Initial con. of TC (ppm)	30	50	70
Catalyst con. (ppm)	50	100	150
H_2O_2 con. (ppm)	0.1	0.3	0.5

General procedure for photocatalytic degradation of TC

Figure 3 shows one schematic diagram of photocatalytic reactor used in the work. An MDF box was designed inside which a circular Pyrex reactor with 300 ml capacity was placed. On the upper section of the box, three mercury lamps (Philips 15 W) were built-in as UV light sources. The radiation is generated almost exclusively at 254 nm. These lamps were set up with the same intervals, so light was evenly radiated on the whole liquid surface inside the reactor. The liquid inside the reactor was agitated by magnetic stirrer and the air inside the box was conditioned by a fan (built-in at back of box). In order to carry out each experiment (according to Table 2), firstly 250 ml TC solution was made as specified concentration and poured inside the reactor. Then, at related pH, the specified amount of photocatalyst and H_2O_2 were added to the solution inside the reactor. In all experiments, pH adjustment was done via minimum use of H_2SO_4 and NaOH. Then, stirrer and UV lamps were immediately turned on to initiate the process. Sampling was done by a 5 ml syringe, every 10 min. To fully separate the catalyst from solution, the samples were centrifuged for 3 min with 3500 rpm speed. The TC concentration of the samples was determined using a UV/Vis spectrophotometer at $\lambda_{max} = 357$ nm. The percentage of initial concentration of pollutant decomposed by the photocatalytic process or the percent of photodegradation efficiency ($x\%$) as a function of time is given by

$$x\% = \frac{C_0 - C}{C_0} \times 100 \quad (2)$$

where C_0 and C are the concentration of TC (ppm) at $t = 0$ and t, respectively.

Table 2 Experimental conditions for photocatalytic process

Exp. no.	Variables			
	pH	Initial con. of TC (ppm)	Catalyst con. (ppm)	H_2O_2 con. (ppm)
1	–1	–1	–1	–1
2	+1	–1	+1	+1
3	–1	–1	+1	–1
4	–1	+1	+1	–1
5	+1	+1	+1	–1
6	0	0	0	0
7	+1	–1	+1	–1
8	–1	+1	–1	+1
9	+1	–1	–1	–1
10	+1	+1	+1	+1
11	–1	+1	–1	–1
12	+1	–1	–1	+1
13	+1	+1	–1	–1
14	–1	+1	+1	+1
15	+1	+1	–1	+1
16	0	0	0	0
17	–1	–1	+1	+1
18	0	0	0	0
19	–1	–1	–1	+1

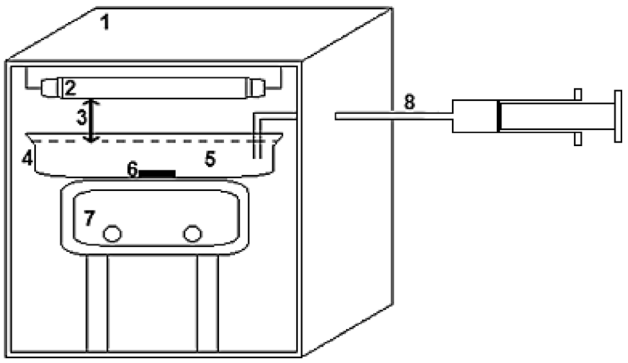

Fig. 3 Schematic diagram of photocatalytic reactor. *1* MDF box, 50 × 50 × 50 cm; *2* Mercury lamps, Philips 15 W; *3* The distance between surface of TC solution and lamps, 5 cm; *4* Reactor, 300 ml capacity; *5* TC solution, 250 ml; *6* Magnet; *7* Magnetic stirrer; *8* Sampling port

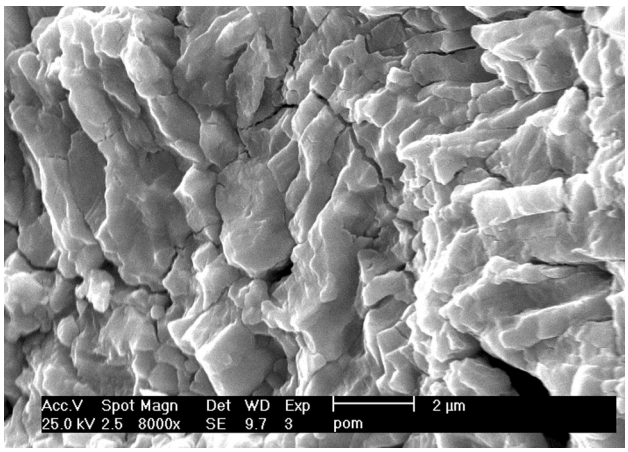

Fig. 4 SEM image of the synthesized 12-TSA·$7H_2O$

Results and discussion

Characterization

The synthesized 12-TSA·$7H_2O$

SEM image of the synthesized 12-TSA·$7H_2O$ is shown in Fig. 4. Surface morphology of 12-TSA·$7H_2O$ shows that this product has suitable structural properties and can be regarded as a catalyst support. In other words, the pores existed on the surface of this catalyst support provide a suitable condition to support α-Fe_2O_3 NPs. IR is a suitable method for the structural characterization of HPAs [26]. FTIR spectrum of the synthesized 12-TSA·$7H_2O$ has been shown in Fig. 5a. There are four kinds of oxygen atoms in 12-TSA·$7H_2O$ structure, 4 Si–O_a in which one oxygen atom connects to Si, 12 W–O_b–W oxygen bridges (corner-sharing oxygen-bridge between different W_3O_{13} groups), 12 W–O_c–W oxygen bridges (edge-sharing oxygen-bridge within W_3O_{13} groups) and 12 W=O_d terminal oxygen atoms. The symmetric and asymmetric stretching

of the different kinds of W–O bonds are observed in the following spectral regions: Si–O_a bonds (1020 cm^{-1}), W = O_d bonds (1000–960 cm^{-1}), W–O_b–W bridges (890–850 cm^{-1}), W–O_c–W bridges (800–760 cm^{-1}) [43]. In Table 3, vibrational frequencies of the synthesized 12-TSA·7H_2O and equivalent values reported in previous studies [43, 44] have been listed. Comparing the vibrational frequencies reveals that 12-TSA·7H_2O has been well synthesized. XRD is one of the most important characterization tools used in solid state chemistry and materials science. Figure 6a shows the XRD pattern of the synthesized 12-TSA·7H_2O. This pattern indicates that the characteristic peaks corresponded to the 12-TSA were well appeared and it means that the synthesized 12-TSA·7H_2O crystals were well formed [44].

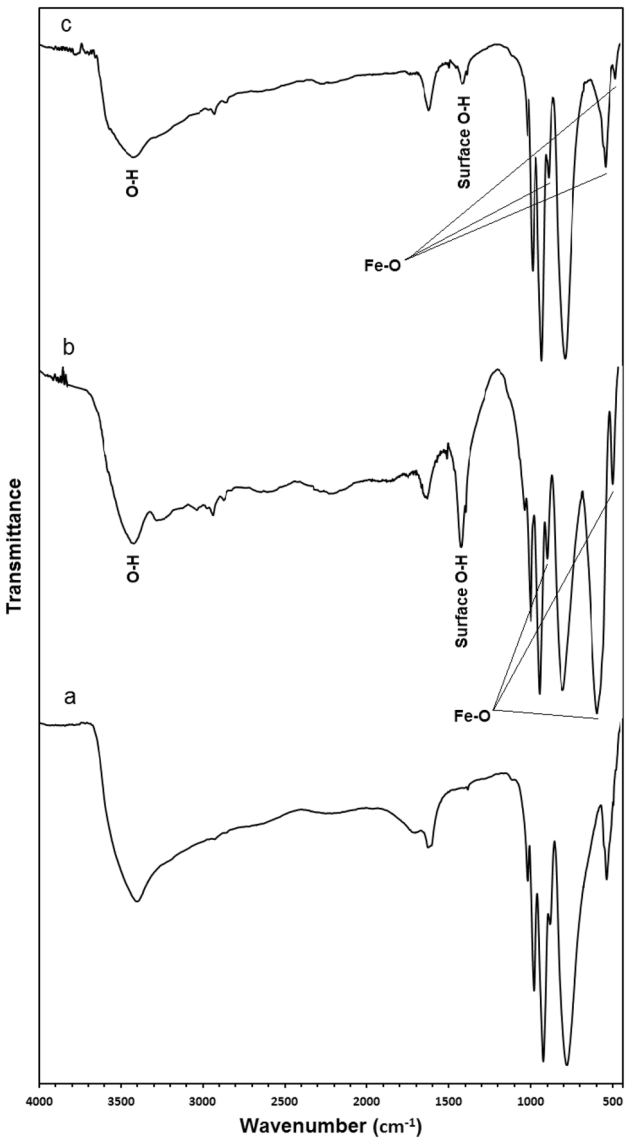

Fig. 5 FTIR spectra of the synthesized 12-TSA·7H_2O (*a*) and α-Fe_2O_3/12-TSA·7H_2O prepared by SSD (*b*) and FHRC (*c*) methods

The prepared α-Fe_2O_3/12-TSA·7H_2O

Figures 7 and 8 show SEM/EDX images of α-Fe_2O_3/12-TSA·7H_2O prepared by SSD and FHRC methods, respectively. These images indicate that in both methods, α-Fe_2O_3 particles were spherically supported on the surface of 12-TSA·7H_2O. The spheres in SSD method are bigger and have covered more area of 12-TSA·7H_2O than that of FHRC method. Possibly in SSD method, spherical α-Fe_2O_3 particles are adhered to each other and bigger spheres have formed while it did not occur in FHRC method and α-Fe_2O_3 particles were separately supported. It is assumed that the causes of this phenomena are as follows: (1) possibly, α-Fe_2O_3 synthesized particles by SSD method are smaller than that of FHRC method and this contributed to their adherence, (2) Supporting through SSD method is done in solid state and this increases the possibility of particles adhering to each other and forming bigger spheres and (3) supporting through FHRC method is done in liquid phase, so the particles could freely move and be separately fixed on the 12-TSA·7H_2O surface. In Fig. 5b, c, FTIR spectra of α-Fe_2O_3/12-TSA·7H_2O prepared by SSD and FHRC methods have been shown, respectively. It is clear that absorption peaks of 12-TSA·7H_2O have appeared without considerable change in the wavenumbers (only their intensities have been slightly changed). It means that in both methods, 12-TSA·7H_2O was stable and it had not been changed chemically during preparing α-Fe_2O_3/12-TSA·7H_2O. Also, absorption peaks of α-Fe_2O_3 have well appeared and are in agreement with results of Bharati et al. [21]. These absorption peaks which are related to stretching and bending modes of OH and Fe–O binding in FeOOH, in some cases overlapped with absorption peaks of 12-TSA·7H_2O. Comparing FTIR spectra reveals that absorption peaks of α-Fe_2O_3 related to SSD method are more intense than that of FHRC method. This partly confirms the results of SEM images. Hence in SSD method, surface of 12-TSA·7H_2O has been covered by more α-Fe_2O_3 particles. In Fig. 6b, c, XRD patterns of α-Fe_2O_3/12-TSA·7H_2O prepared by SSD and FHRC methods have been illustrated, respectively. In both of these patterns, characteristic peaks of 12-TSA·7H_2O have well appeared which indicates that 12-TSA·7H_2O was stable during the supporting process in both SSD and FHRC methods. In these patterns, the characteristic peaks of α-Fe_2O_3 which have also been marked have appeared and it is in agreement with results of Bharati et al. [21]. In XRD related to SSD method, intensity of 12-TSA·7H_2O and α-Fe_2O_3 characteristic peaks is lower and higher than that of FHRC method, respectively. This issue confirms the results of SEM and FTIR, so during supporting through SSD method, 12-TSA·7H_2O surface has been covered by the greater amount of α-Fe_2O_3 particles. The size of spherical α-Fe_2O_3

Table 3 Vibrational frequencies of the synthesized 12-TSA·$7H_2O$ and equivalent values reported in previous reports

Number	The synthesized 12-TSA·$7H_2O$		[43, 44]
	Wavenumber (cm^{-1})	Transmittance %	
1	1019.04	13.29	1020 (weak)
2	980.68	8.81	981 (sharp)
3	924.31	5.92	928 (very sharp)
4	882.63	11.52	880 (medium)
5	780.28	5.77	785 (very sharp)
6	537.41	13.35	540 (medium)

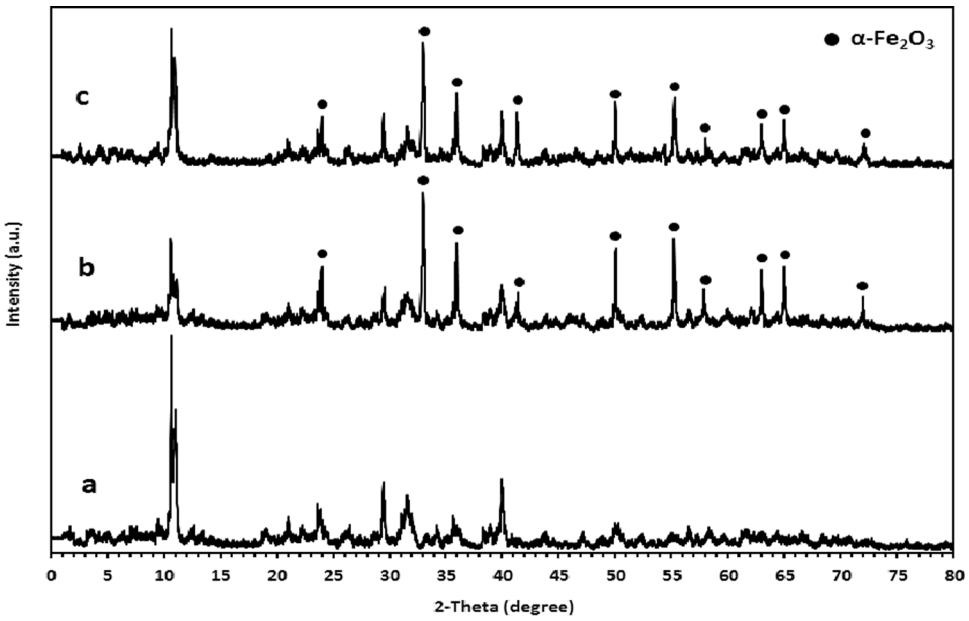

Fig. 6 X-ray diffractogram of the synthesized 12-TSA·$7H_2O$ (*a*), α-Fe_2O_3/12-TSA·$7H_2O$ prepared by SSD (*b*) and FHRC (*c*) methods

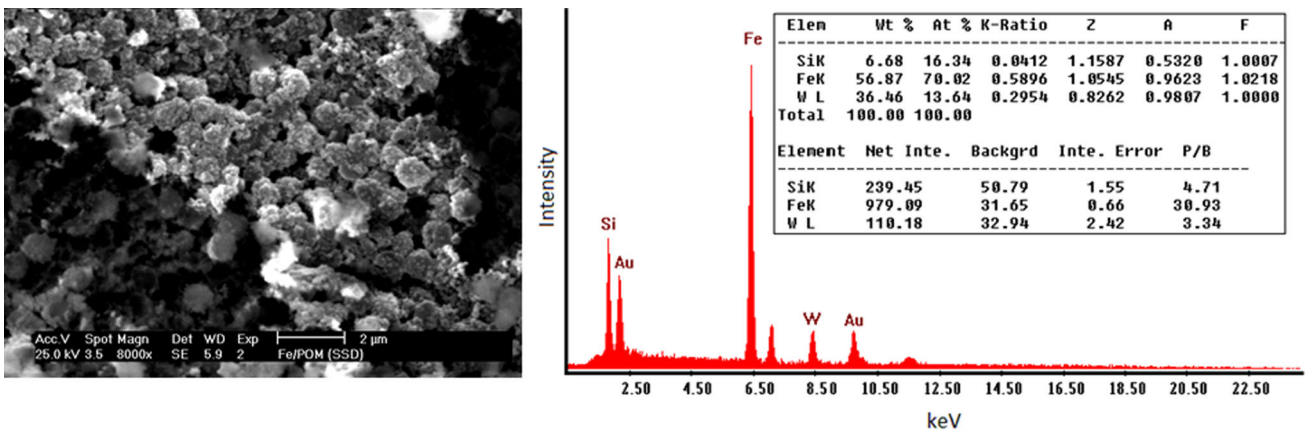

Fig. 7 SEM image and EDX results of α-Fe_2O_3/12-TSA·$7H_2O$ prepared by SSD method

particles supported on the surface of 12-TSA·$7H_2O$ were calculated using XRD and Warren–Averbach method (taking account of device errors) whose averages for SSD and FHRC methods were 50.5 and 70.82 nm, respectively. The BET surface area of catalyst prepared by SSD and FHRC methods were determined 57.53 and 39.84 (m^2/g), respectively. It seems that the high amount of iron oxide formed on the base has been increase the BET surface area of catalyst prepared with SSD method.

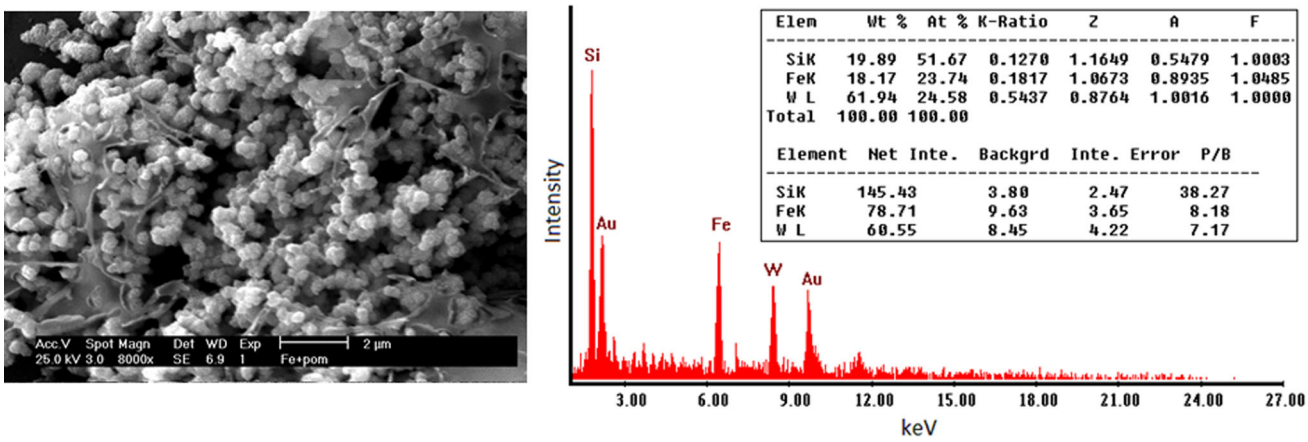

Fig. 8 SEM image and EDX results of α-Fe_2O_3/12-TSA·$7H_2O$ prepared by FHRC method

UV/Vis spectra

The absorbance of TC solutions during photocatalytic process (using α-Fe_2O_3/12-TSA·$7H_2O$ prepared by SSD method and according to exp. no. 8) at initial and after 10, 20, 30, 40 and 50 min irradiation time verses wavelength are depicted in Fig. 9. In all experiments, *x*% was calculated at $\lambda_{max} = 357$ nm. The wavelength of maximum absorbance (in 357 nm) did not change with time, then this wavelength for measuring the concentration of pollutants was chosen. Furthermore, absorbance changes in 357 nm were completely regular and measurable.

Performance of photocatalysts

Having carried out all experiments based on Table 2, *x*% values were calculated at $\lambda_{max} = 357$ nm following 50 min after reaction which have been reported in Table 4. In general, comparing *x*% values reveals that the degree of TC photocatalytic degradation by pure α-Fe_2O_3 is lower than that of α-Fe_2O_3/12-TSA·$7H_2O$ prepared through SSD and FHRC methods. This means that supporting α-Fe_2O_3 NPs leads to increase their photocatalytic activity. Also, comparing the results of SSD and FHRC methods indicates that α-Fe_2O_3/12-TSA·$7H_2O$ prepared through SSD method was effective from the aspect of TC photocatalytic degradation and has yielded more *x*% values. Comparing *x*% values in one series of experiments (1 through 19) shows that the highest degradation percentage has been obtained in exp. no. 7. To better compare the results, *x*% histogram versus experiment number for pure α-Fe_2O_3 and α-Fe_2O_3/12-TSA·$7H_2O$ prepared through SSD and FHRC methods has been shown in Fig. 10. The histogram clearly indicates that in all experiments α-Fe_2O_3 NPs supported on the surface of 12-TSA·$7H_2O$ (particularly through SSD method) had more photocatalytic efficacy and has degraded more TC.

Photocatalytic mechanism

According to exp. no. 7, the effects of UV irradiation, pure α-Fe_2O_3 NPs and α-Fe_2O_3/12-TSA·$7H_2O$ prepared by two different SSD and FHRC methods on the photodegradation

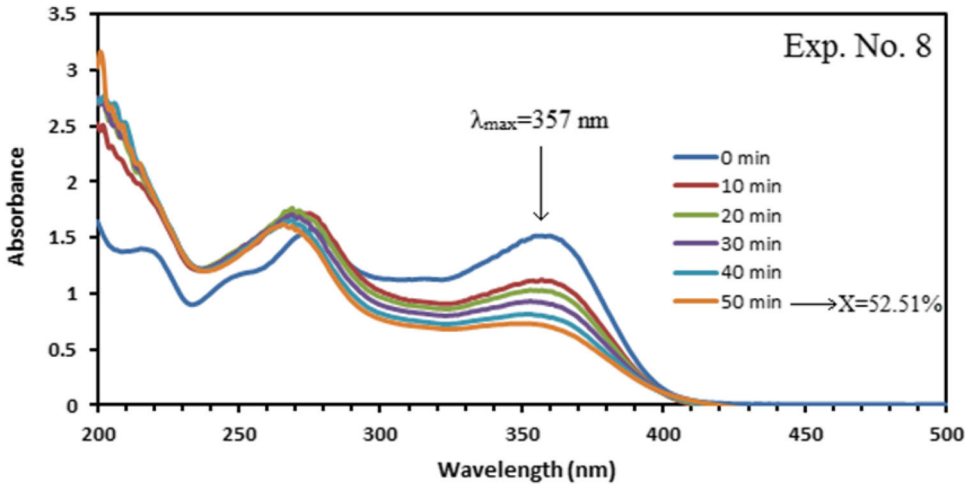

Fig. 9 UV/Vis spectral absorption changes of TC solution photodegraded by α-Fe_2O_3/12-TSA·$7H_2O$ prepared through SSD method (pH 4, Initial concentration of TC = 70 ppm, catalyst concentration = 50 ppm, H_2O_2 concentration = 0.5 ppm)

Table 4 *x%* values after 50 min photodegradation process at $\lambda_{max} = 357$ nm

Exp. no.	*x%*		
	Pure α-Fe_2O_3 NPs	α-Fe_2O_3/12-TSA·7H_2O prepared by SSD method	α-Fe_2O_3/12-TSA·7H_2O prepared by FHRC method
1	64.11	78.59	66.32
2	75.39	93.61	85.95
3	67.56	85.35	73.29
4	48.83	62.74	53.22
5	37.14	60.51	45.07
6	36.97	69.61	60.38
7	82.17	97.39[a]	88.44
8	37.95	52.51	42.66
9	65.46	84.34	74.61
10	44.37	58.94	47.92
11	32.84	47.91	38.91
12	62.00	91.48	74.28
13	29.84	47.06	37.71
14	40.69	62.45	48.72
15	39.31	55.34	45.62
16	37.02	69.75	59.79
17	66.83	82.21	77.13
18	36.83	69.44	60.13
19	65.83	87.17	81.84

[a] Maximum value of *x%*

of TC are presented in Fig. 11. This Figure designates that in the presence of α-Fe_2O_3/12-TSA·7H_2O prepared by SSD method and UV irradiation 97.39% of TC was degraded at the reaction time of 50 min while it was 88.44, 82.17 and 10.2% for α-Fe_2O_3/12-TSA·7H_2O prepared by FHRC method, pure α-Fe_2O_3 NPs and only UV, respectively. When α-Fe_2O_3 is illuminated by the light, electrons are promoted from the valence band (VB) to the conduction band (CB) of the semi conducting oxide to give electron–hole pairs. The VB potential (h_{VB}) is positive enough to generate hydroxyl radicals at the surface, and the CB potential (e_{CB}) is negative enough to reduce molecular oxygen. The hydroxyl radical is a powerful oxidizing agent and attacks TC molecules present at or near the surface of α-Fe_2O_3. It causes the photo-oxidation of TC according to the following reactions [45–50]:

$$\alpha\text{-}Fe_2O_3 + h\nu \rightarrow \alpha\text{-}Fe_2O_3(e^-_{CB} + h^+_{VB})$$
$$h^+_{VB} + H_2O_{(ads)} \rightarrow H^+ + {}^{\cdot}OH^-_{(ads)}$$
$$h^+_{VB} + OH^-_{(ads)} \rightarrow {}^{\cdot}OH_{(ads)}$$
$$e^-_{CB} + O_{2(ads)} \rightleftarrows {}^{\cdot}O^-_{2(ads)}$$
$$H_2O \rightleftarrows H^+ + OH^-$$
$${}^{\cdot}O^-_{2(ads)} + H^+ \rightarrow {}^{\cdot}HO_2$$
$$2\,{}^{\cdot}HO_2 \rightarrow H_2O_2 + O_2$$
$$H_2O_2 + \alpha\text{-}Fe_2O_3(e^-_{CB}) \rightarrow {}^{\cdot}OH + OH^- + \alpha\text{-}Fe_2O_3$$
$${}^{\cdot}OH_{(ads)} + TC \rightarrow \text{degradation of TC}$$
$$h^+_{VB} + TC\ TC^{\cdot+} \rightarrow \text{oxidation of TC.}$$

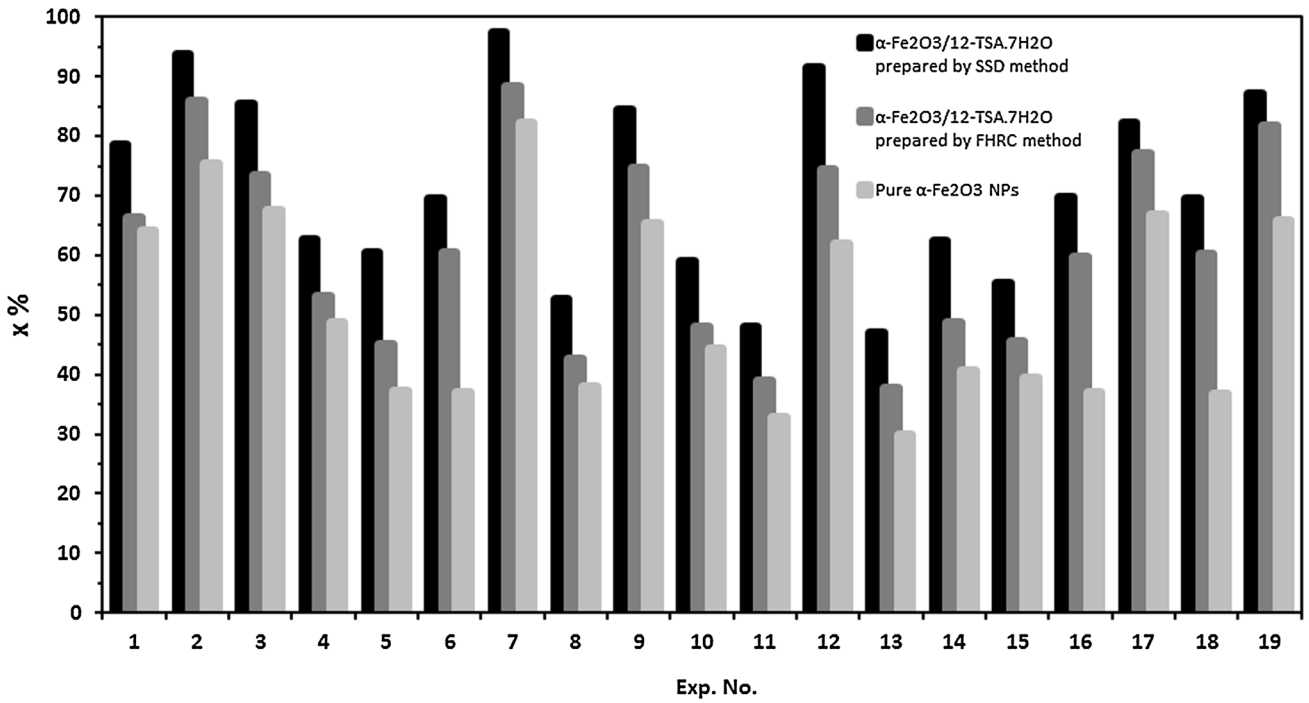

Fig. 10 *x%* values versus experiment number

The mechanism is summarized in Fig. 12. The main role of the foundation is creating the perfect conditions for putting the TC and hydroxyl radical beside each other. Photocatalytic activity increased after stabilizing iron oxide on 12-TSA·7H_2O. To comment on this result, we propose that the hydroxyl radicals, on the surface of iron oxide, are easily transferred onto the surface of 12-TSA·7H_2O. That means the organic pollutants such as TC, which have already been adsorbed on the nonphotoactive 12-TSA·7H_2O, have chances to be degraded due to the appearance of hydroxyl radicals, resulting in the enhancement of the photodegradation performance of α-Fe_2O_3/12-TSA·7H_2O (as shown in Fig. 12b).

Kinetics of photocatalytic degradation of TC

Figure 13 displays the plot of $\ln(C_0/C)$ versus reaction time for TC. The linearity of the plot suggests that the photodegradation reaction approximately follows the pseudo-first order kinetics with a rate coefficient $k = 0.0098\ \text{min}^{-1}$.

The statistical analysis (optimum conditions)

Since α-Fe_2O_3 NPs supported through SSD method have shown more effective than other photocatalysts from the view of the TC photocatalytic degradation, then in this section we carry out the statistical results analysis of the photocatalytic process in which α-Fe_2O_3/12-TSA·7H_2O prepared by SSD method has been utilized. Analysis of variance (ANOVA) is a set consists of a number of statistical methods used to analyze the differences among group means and their associated procedures. ANOVAs are useful for testing three or more means variables for statistical significance. ANOVA was used for graphical analyses of the data to obtain the interaction between the process variables and the responses. The quality of the fit polynomial model was expressed by the coefficient of determination R^2, and its statistical significance was checked by the Fisher's F test in the same program. Model terms were evaluated by the P value. In Table 5, the estimated effects and coefficients for $x\%$ have been listed. In this table, standard deviation (S), correlation coefficient, pried R^2 and adjusted R^2 values were also reported. The square of the correlation coefficient for each response was computed as the coefficient of determination (R^2). The accuracy and variability of the model can be evaluated by R^2. The R^2 value is always between 0 and 1. The closer the R^2 value to 1, the stronger the model is and the better the model predicts the response ($x\%$). R^2 value was reported to be 0.9915 in this paper. The "pried R^2" of 0.9662 is in reasonable agreement with the "adj R^2" of 0.9848,

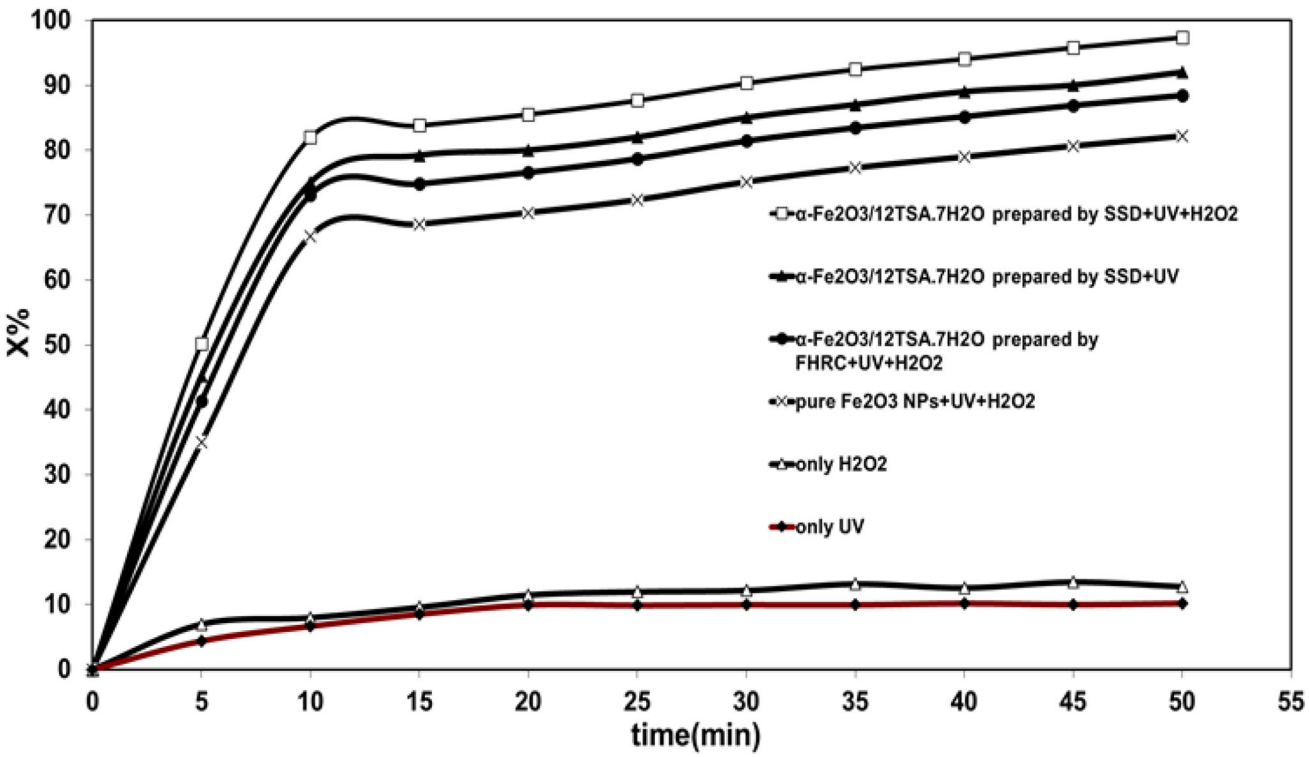

Fig. 11 Effect of UV light, pure α-Fe_2O_3 NPs and α-Fe_2O_3/12-TSA·7H_2O prepared by FHRC and SSD methods on TC degradation (pH 8, Initial concentration of TC = 30 ppm, catalyst concentration = 150 ppm, H_2O_2 concentration = 0.1 ppm)

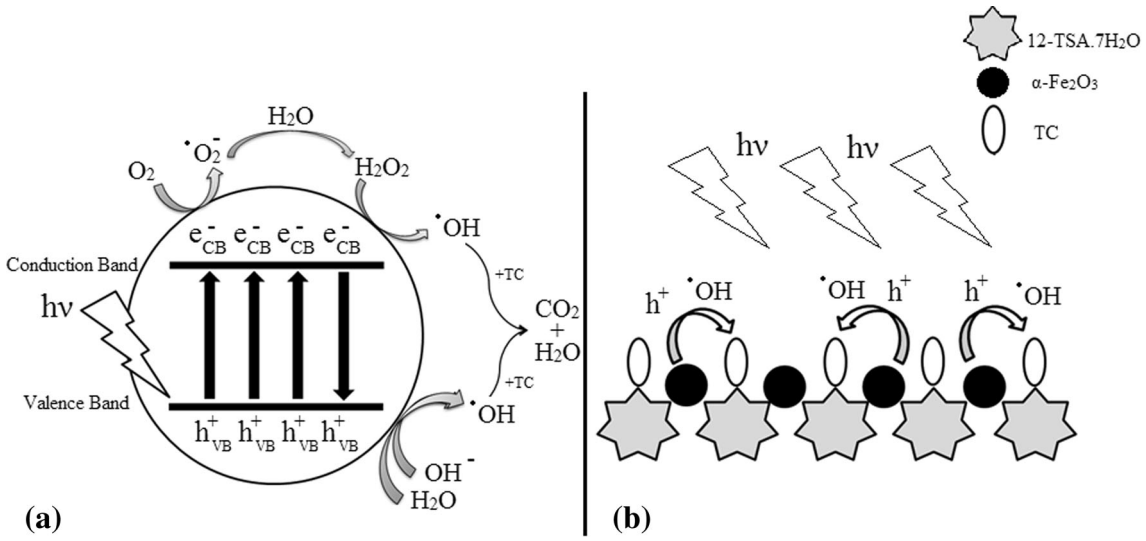

Fig. 12 General mechanism of the photocatalysis (**a**) and photocatalytic activity of α-Fe_2O_3/12-TSA·$7H_2O$ (**b**)

confirming good predictability of the model. Due to Table 5 and the significant variables effects on the response, affect magnitudes of the initial concentration of TC, pH, H_2O_2 concentration and catalyst concentration equal to 31.59, 3.72, 2.48 and 7.35, respectively. Thus, the significant reaction parameters were (the most to the least significant): initial concentration of TC > catalyst concentration > pH > and H_2O_2 concentration. Of course, it is necessary to note that despite other three variables, the variable of the initial concentration of TC has a negative effect on the response (−31.59). This means that increasing the initial concentration of TC leads to decrease *x*% and conversely. In this way, the effects about the variables interaction were reported in Table 5. As can be seen from these results, it is the only interaction of variables, namely the initial concentration of TC and the catalyst concentration which have positive effects (3.10). The interaction of the initial concentration of TC with pH and the interaction of H_2O_2 concentration with catalyst concentration have

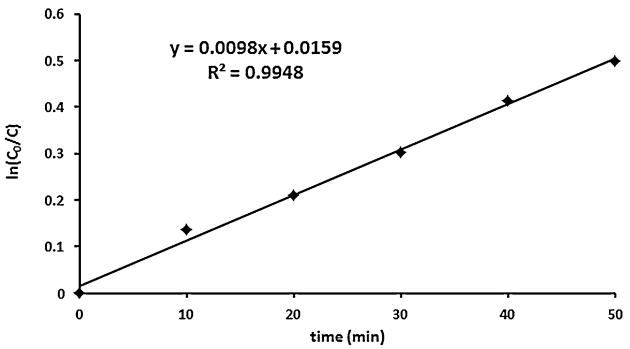

Fig. 13 Plot of reciprocal of pseudo-first order rate constant against initial concentration of TC = 70 ppm, catalyst concentration = 50 ppm, H_2O_2 concentration = 0.5 ppm and pH 4

both negative and roughly the same effects on the *x*% value (−4.67 and −4.66, respectively). In Table 5, the coefficients of each term have been reported which are the same term coefficients in response function which they will be given in the following. It is vital to note that P values have been assessed considering Alpha (α) = 0.05. Table 6 depicts the results of ANOVA. The effect on the response was increased by increasing the value of F parameter and decreasing *P* parameter. For main effects (with 4 degrees of freedom) including the initial concentration of TC, pH, H_2O_2 concentration and catalyst concentration, *F* and *P* values have obtained as 278.34 and <0.0001, respectively. Besides, these values were 18.41 and <0.0001 for 2-way interactions (with 3 freedom degree), respectively. In Table 7, complementary results have been listed which have been used for drawing residual plots. Residual values were calculated from subtracting experimental *x*% values and fitted values.

In order to compare the variables effect (from the viewpoint of magnitude) on the response, the Fig. 14a could be investigated which is one Pareto chart of the standardized effects. In this Figure, those variables whose effects on response is negative (−) or positive (+) have been marked. The results revealed that the effect of the initial concentration of TC on the *x*% is greater than other variables effect (at least three times) but the effect of this variable is negative i.e. increasing or decreasing the initial concentration of TC leads to decrease and increase *x*%, respectively. In order to better investigate the residual values, residual plot versus exp. no. has been illustrated in Fig. 14b. As it is seen, eight points (residuals) are located under zero line (negative), nine points above zero line (positive) and two points roughly on the zero line. Due to this and comparing distance of points from zero line, it

Table 5 Estimated effects and coefficients for *x*%

Term	Effect	Coef	SE Coef	*T* (Coef/SE Coef)	*P* value	Result
Constant	–	71.73	0.4905	146.22	<0.0001	Significant
Initial con. of TC	–31.59	–15.79	0.4905	–32.19	<0.0001	Significant
pH	3.72	1.86	0.4905	3.79	0.004	Significant
H_2O_2 con.	2.48	1.24	0.4905	2.52	0.03	
Catalyst con.	7.35	3.68	0.4905	7.49	<0.0001	Significant
Initial con. of TC × pH	–4.66	–2.33	0.4905	–4.75	0.001	Significant
Initial con. of TC × catalyst con.	3.10	1.55	0.4905	3.16	0.010	
H_2O_2 con. × catalyst con.	–4.67	–2.34	0.4905	–4.76	0.001	Significant
Center point	–	–2.13	1.2345	–1.72	0.116	

$S = 1.96219$, $R^2 = 99.15\%$, Pred $R^2 = 96.62\%$, Adj $R^2 = 98.48\%$

Table 6 ANOVA results

Source	Degree of freedom	Seq SS	Adj SS	Adj MS	*F* value
Initial con. of TC	1	3990.68	3990.68	3990.68	1036.49
pH	1	55.25	55.25	55.25	14.35
H_2O_2 con.	1	24.54	24.54	24.54	6.37
Catalyst con.	1	216.12	216.12	216.12	56.13
Initial con. of TC × pH	1	86.73	86.73	86.73	22.53
Initial con. of TC × catalyst con.	1	38.55	38.55	38.55	10.01
H_2O_2 con. × catalyst con.	1	87.36	87.36	87.36	22.69

could be said that residual distribution is normal. An extremely useful procedure is to construct a normal probability plot of the residuals. If the underlying error distribution is normal, this plot will resemble a straight line. Figure 14c shows normal probability plot. In this plot, it is fully clear that residuals distribution is normal because points (especially central points) are close to straight line. If the model is correct and if the assumptions are satisfied, the residuals should be structureless; in particular, they should be unrelated to any other variable including the predicted response. A simple check is to plot the residuals versus the fitted values. Figure 14d displays plot of residuals versus fitted values. Mathematical model representing TC photocatalytic degradation in the range studied can be expressed by the following equation:

$$\begin{aligned}\text{Response} &= x\% \\ &= 71.73 - 15.79A + 1.86B + 1.24C \\ &\quad + 3.68D - 2.33AB + 1.55AD - 2.34CD\end{aligned}$$

where *A*, *B*, *C* and *D* are the initial concentration of TC, pH, H_2O_2 concentration and catalyst concentration, respectively.

In Fig. 15, the plots of main effects have been shown. These plots indicate that of four main effects, only the

Table 7 Residual values

Exp. no.	*x*%	Fit	SE fit	Residual (*x*%–fit)	St resid
1	78.59	77.6338	1.3875	0.9562	0.69
2	93.61	92.7296	1.3875	0.8804	0.63
3	85.35	86.5531	1.3875	–1.1977	–0.86
4	62.74	62.7282	1.3875	0.0118	0.01
5	60.51	61.7882	1.3875	–1.2782	–0.92
6	69.61	69.6000	1.1329	0.0100	0.01
7	97.39	94.9260	1.3875	2.4640	1.78
8	52.51	54.7502	1.3875	–2.2402	–1.61
9	84.34	86.0067	1.3875	–1.6667	–1.20
10	58.94	59.5918	1.3875	–0.6518	–0.47
11	47.91	47.5998	1.3875	0.3102	0.22
12	91.48	93.1572	1.3875	–1.6778	–1.21
13	47.06	46.6598	1.3875	0.4002	0.29
14	62.45	60.5318	1.3875	1.9182	1.38
15	55.34	53.8102	1.3875	1.5298	1.10
16	69.75	69.6000	1.1329	0.1500	0.09
17	82.21	84.3567	1.3875	–2.1467	–1.55
18	69.44	69.6000	1.1329	–0.1600	–0.10
19	87.17	84.7843	1.3875	2.3882	1.72

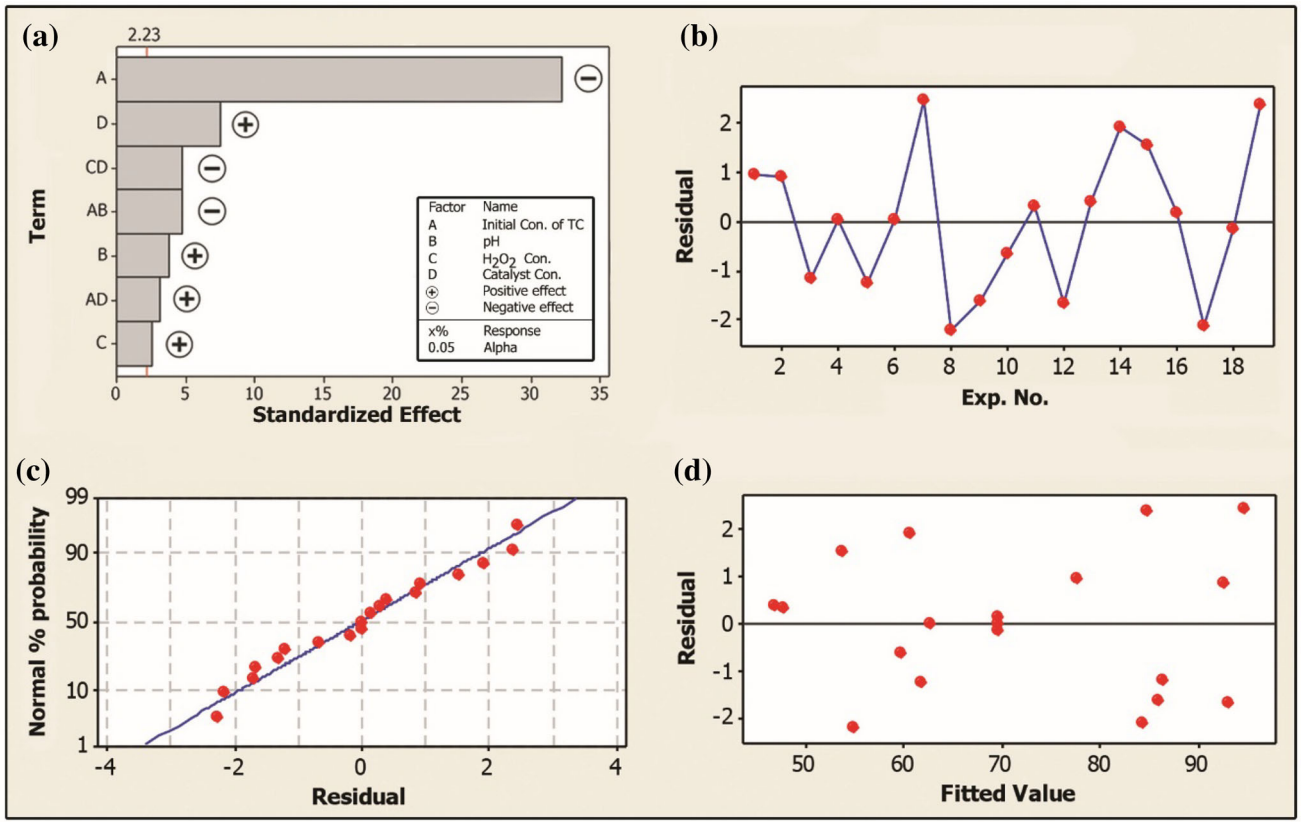

Fig. 14 **a** Pareto chart of the standardized effects, **b** plot of residuals versus exp. no., **c** Normal probability plot and **d** plot of residuals versus fitted values

variable of the initial concentration of TC has a negative effect on response ($x\%$); effects of other variables on response were positive. In effect, increasing the initial concentration of TC and decreasing pH, H_2O_2 concentration and catalyst concentration will be caused to decrease and increase $x\%$, respectively (if the interaction effect of variable is ignored). The slope of line in main effect plots is one indicator of magnitude related to the variable effect on the response. Therefore, the order of affecting variables from magnitude viewpoint is as initial concentration of TC > catalyst concentration > pH > H_2O_2 concentration which confirm the results of Fig. 14a.

In Fig. 16, interaction plots for $x\%$ have been presented. Generally, in such plots the more parallel the lines, the lower the interaction effect would be and the more intersecting the lines, the higher the interaction effect would be. As it is observed, there is a significant interaction effect among catalyst concentration and H_2O_2 concentration variables. This effect is slightly found at interaction among pH and catalyst concentration variables. Figure 17 shows a cube plot for $x\%$. Using this plot, one could easily identify the conditions for reaching the desirable $x\%$. For example, in order to reach maximum degradation ($x\% = 97.39$) the variables of pH, the initial concentration of TC, catalyst concentration and H_2O_2 concentration should be at levels of $+1(8)$, $-1(30$ ppm), $+1(150$ ppm) and $-1(0.1$ ppm), respectively. Generally, considering the interaction effects is very important because it may place the unpredictable effects on the response. For example, based on the results of Fig. 15 even though H_2O_2 concentration had simply a positive effect on $x\%$, the maximum $x\%$ was achieved in those conditions where H_2O_2 concentration was at its minimum level (see exp. no 7 in Table 4). For the same reason, the interaction effect of variables should not be ignored in studying variables for reaching optimal conditions.

Finally, to determine the stability of the catalyst after 5 steps photocatalytic decomposition process, catalyst separation and then drying it, the FTIR spectrum of the sample showed that the catalyst structure have not changed. To determine the reusability of catalyst, 5 times was repeated experiment in the optimal conditions. Results, respectively, are as follows: X1 = 97.39, X2 = 97.32, X3 = 97.24, X4 = 97.20, X5 = 97.21. These results show that reusability of catalyst is appropriate.

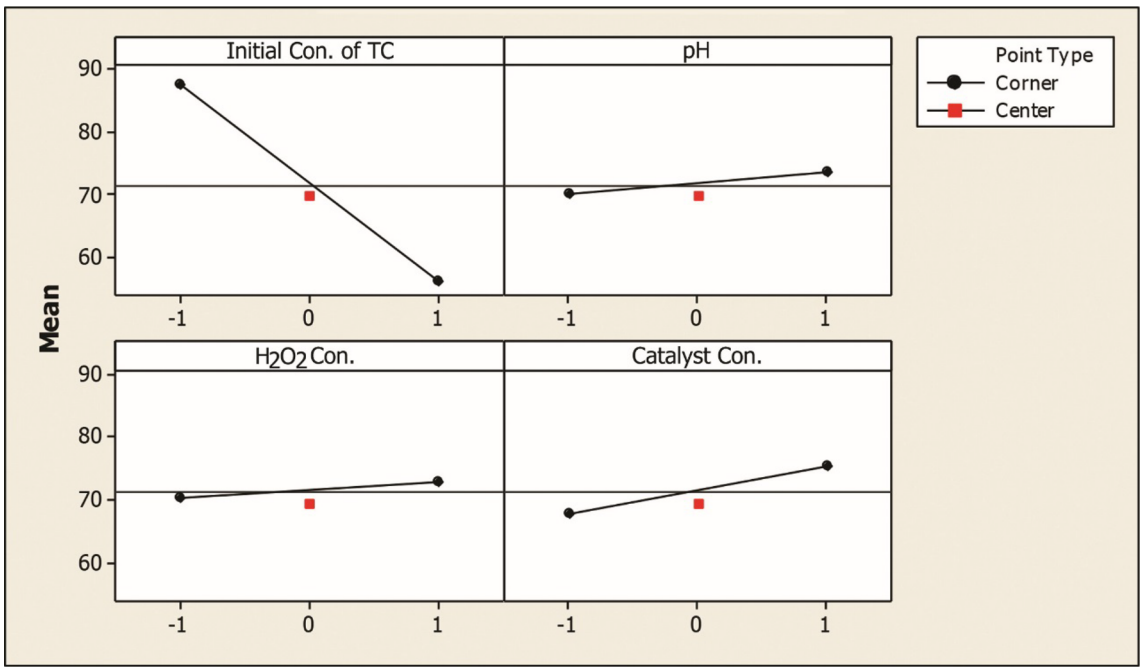

Fig. 15 Main effects plot for *x*%

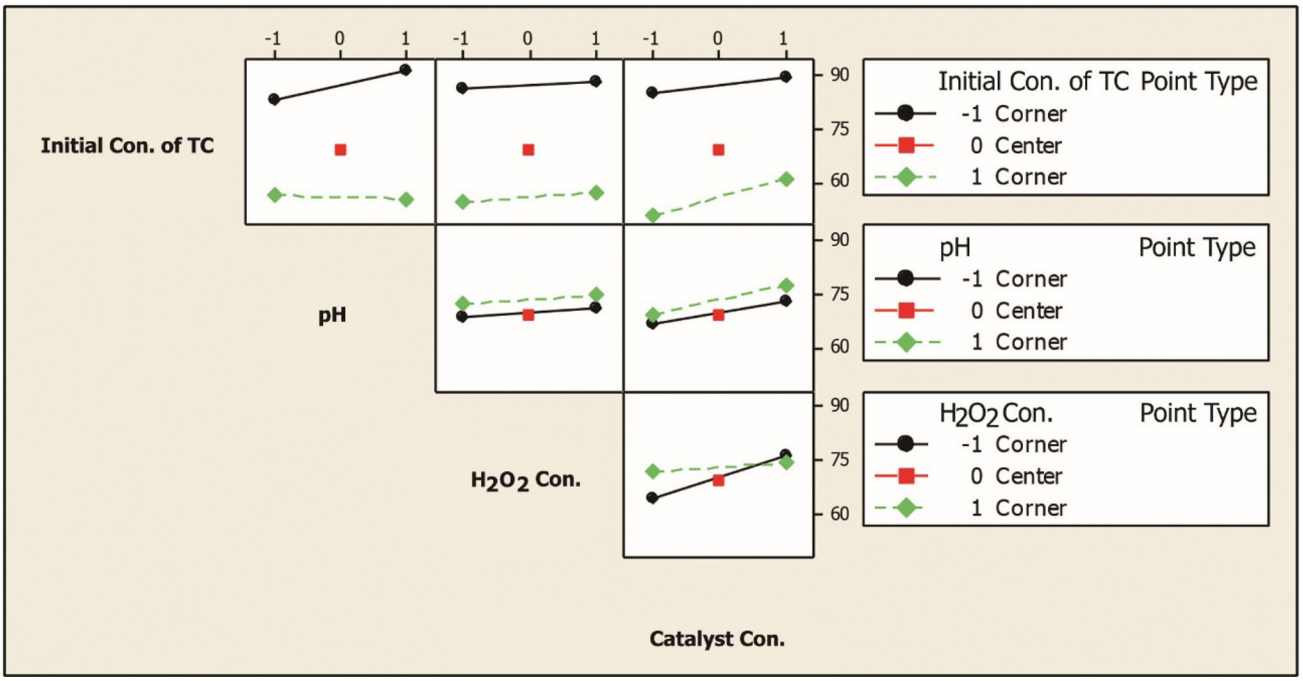

Fig. 16 Interaction plot for *x*%

Conclusions

The results revealed that:

1. Spherical α-Fe_2O_3 NPs had been successfully synthesized and supported on the surface of 12-TSA·$7H_2O$ through SSD and FHRC methods with no decrease of NPs photocatalytic efficiency and chemical change of 12-TSA·$7H_2O$ which are indicative of being effective these supporting methods.
2. While supporting α-Fe_2O_3 NPs on the surface of 12-TSA·$7H_2O$ help to recover them from the medium and reusing them, it causes to enhance their photocatalytic activities.

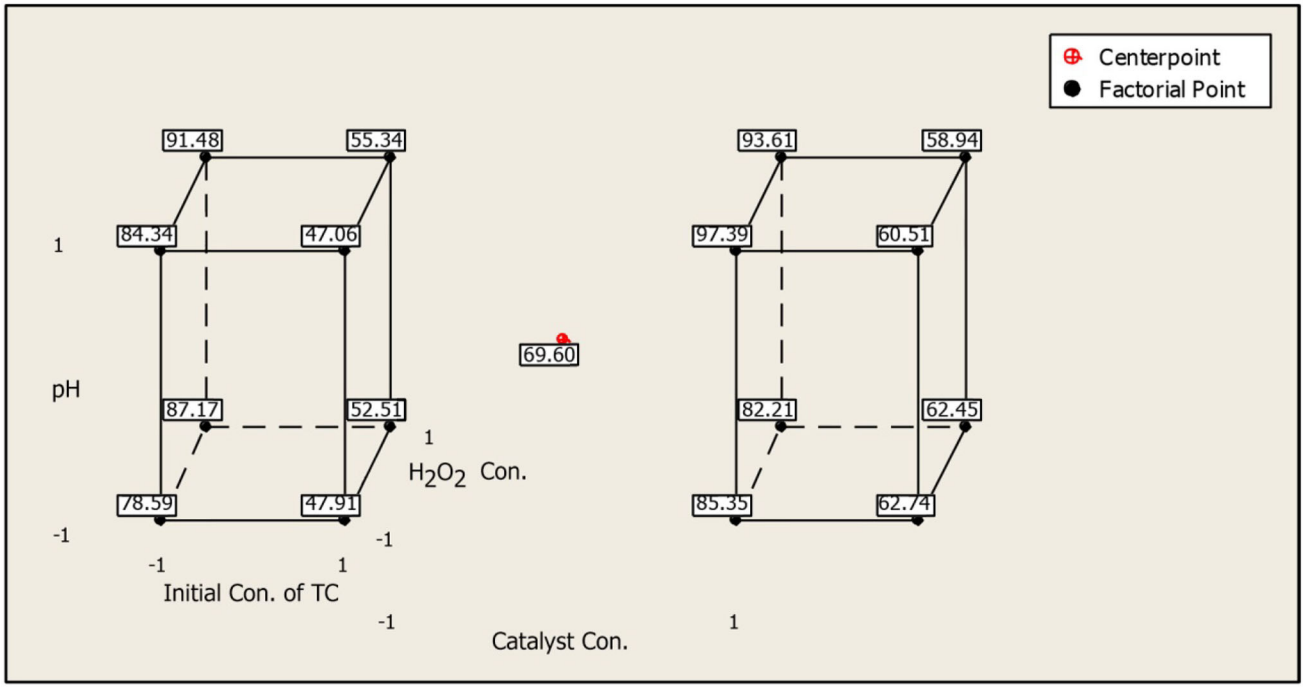

Fig. 17 Cube plot (data means) for *x*%

3. Nanophotocatalytic effect of α-Fe_2O_3/12-TSA·7H_2O prepared through SSD and FHRC methods on the TC degradation is greater than pure α-Fe_2O_3 NPs.
4. As shown in the analysis of EDX, amount of iron oxide supported on the 12-TSA·7H_2O using SSD method is greater than the FHRC method. Then photo-activity of catalyst that prepared with SSD method is higher than FHRC method. Therefore, SSD method is more suitable.
5. The statistical analysis results indicated that the model used in this paper is significantly reliable and valid.
6. In the process of the TC photocatalytic degradation using α-Fe_2O_3/12-TSA·7H_2O prepared though SSD method, four parameters of pH, the initial concentration of TC, catalyst concentration and H_2O_2 concentration are effective on *x*%. If interaction effects of variables are ignored, only the initial concentration of TC has a negative effect on the *x*%.
7. The interaction effects of variables are very important and should be considered for optimizing the conditions because it significantly affects the *x*%. For example, even though H_2O_2 concentration has simply a positive effect on *x*%, interaction effects cause to yield maximum *x*% at conditions where H_2O_2 concentration is at minimum level.
8. The optimum conditions for the TC degradation process by α-Fe_2O_3/12-TSA·7H_2O prepared through SSD is as pH 8, initial concentration of TC = 30 ppm, catalyst concentration = 150 ppm and H_2O_2 concentration = 0.1 ppm so that they cause to reach maximum degradation (97.39%).
9. The kinetics of photocatalytic degradation of TC is of the pseudo-first order with $k = 0.0098\ \text{min}^{-1}$.

Acknowledgements The authors wish to thank the Islamic Azad University of Arak, Iran, for financial support.

References

1. Balcioglu IA, Otker M (2003) Treatment of pharmaceutical wastewater containing antibiotics by O_3 and O_3/H_2O_2 processes. Chemosphere 50:85–95
2. Novo A, Andre S, Viana P, Nunes OC, Manaia CM (2013) Antibiotic resistance, antimicrobial residues and bacterial community composition in urban wastewater. Water Res 47:1875–1887
3. Hou J, Wang C, Mao D, Luo Y (2016) The occurrence and fate of tetracyclines in two pharmaceutical wastewater treatment plants of Northern China. Environ Sci Pollut Res Int 23:1722–1731
4. Kümmerer K (2009) Antibiotics in the aquatic environment—a review-part I. Chemosphere 75:417–434
5. Brown KD, Kulis J, Thomson B, Chapman TH, Mawhinney DB (2006) Occurrence of antibiotics in hospital, residential, and dairy effluent, municipal wastewater, and the Rio Grande in New Mexico. Sci Total Environ 366:772–783

6. Pailler JY, Krein A, Pfister L, Hoffmann L, Guignard C (2009) Solid phase extraction coupled to liquid chromatography-tandem mass spectrometry analysis of sulfonamides, tetracyclines, analgesics and hormones in surface water and wastewater in Luxembourg. Sci Total Environ 407:4736–4743
7. Homem V, Santos L (2011) Degradation and removal methods of antibiotics from aqueous matrices—a review. J Environ Manag 92:2304–2347
8. Xia Y, Xiong Y, Lim B, Skrabalak SE (2009) Shape-controlled synthesis of metal nanocrystals: simple chemistry meets complex physics? Angew Chem Int Ed 48:60–103
9. Jun YW, Choi JS, Cheon J (2007) Heterostructured magnetic nanoparticles: their versatility and high performance capabilities. Chem Commun 12:1203–1214
10. Chen J, Xu L, Li W, Gou X (2005) α-Fe_2O_3 nanotubes in gas sensor and lithium-ion battery applications. Adv Mater 17:582–586
11. Raming TP, Winnubst AJA, Van Kats CM, Philipse AP (2002) The synthesis and magnetic properties of nanosized hematite (α-Fe_2O_3) particles. J Colloid Interface Sci 249:346–350
12. Walter D (2006) Characterization of synthetic hydrous hematite pigments. Thermochim Acta 445:195–199
13. Shekhah O, Ranke W, Schüle A, Kolios G, Schlögl R (2003) Styrene synthesis: high conversion over unpromoted iron oxide catalysts under practical working conditions. Angew Chem Int Ed 42:5760–5763
14. Mishra M, Chun DM (2015) α-Fe_2O_3 as a photocatalytic material: a review. Appl Catal A 498:126–141
15. Farahmandjou M, Soflaee F (2015) Synthesis and characterization of α-Fe_2O_3 nanoparticles by simple co-precipitation method. Phys Chem Res 3:191–196
16. Liang H, Liu K, Ni Y (2015) Synthesis of mesoporous α-Fe_2O_3 via sol–gel methods using cellulose nano-crystals (CNC) as template and its photo-catalytic properties. Mater Lett 159:218–220
17. Diab M, Mokari T (2014) Thermal decomposition approach for the formation of α-Fe_2O_3 mesoporous photoanodes and an α-Fe_2O_3/CoO hybrid structure for enhanced water oxidation. Inorg Chem 53:2304–2309
18. Jiang T, Poyraz AS, Iyer A, Zhang Y, Luo Z, Zhong W, Miao R, El-Sawy AM, Guild CJ, Sun Y, Kriz DA, Suib SL (2015) Synthesis of mesoporous iron oxides by an inverse micelle method and their application in the degradation of orange II under visible light at neutral pH. J Phys Chem C 119:10454–10468
19. Askarinejad A, Bagherzadeh M, Morsali A (2011) Sonochemical fabrication and catalytic properties of α-Fe_2O_3 nanoparticles. J Exp Nanosci 6:217–225
20. Tadic M, Panjan M, Damnjanovic V, Milosevic I (2014) Magnetic properties of hematite (α-Fe_2O_3) nanoparticles prepared by hydrothermal synthesis method. Appl Surf Sci 320:183–187
21. Bharathi S, Nataraj D, Mangalaraj D, Masuda Y, Senthil K, Yong K (2010) Highly mesoporous α-Fe_2O_3 nanostructures: preparation, characterization and improved photocatalytic performance towards Rhodamine B (RhB). J Phys D Appl Phys 43:1–9
22. Chen M, Liu J, Chao D, Wang J, Yin J, Lin J, Fan HJ, Shen ZX (2014) Porous α-Fe_2O_3 nanorods supported on carbon nanotubes-graphene foam as superior anode for lithium ion batteries. Nano Energy 9:364–372
23. Rancourt DG, Julian SR, Daniels JM (1985) Mössbauer characterization of very small superparamagnetic particles; application to intra-zeolitic α-Fe_2O_3 particles. J Magn Magn Mater 49:305–316
24. Nikazar M, Gholivand K, Mahanpoor K (2008) Photocatalytic degradation of azo dye acid red 114 in water with TiO_2 supported on clinoptililite as a catalyst. Desalination 219:293–300
25. Hill CL (1998) Polyoxometalates. Chem Rev 98:1–387
26. Pope MT (1983) Heteropoly and Isopoly Oxometalates. Springer-Verlag, Berlin, Heidelberg
27. Kozhevnikov IV (2012) Catalysis by heteropoly acids and multicomponent polyoxometalates in liquid-phase reactions. Chem Rev 98:171–198
28. Es'haghi Z, Hooshmand S (2015) Dispersive solid-liquid phase microextraction based on nanomagnetic preyssler heteropolyacid: a novel method for the preconcentration of nortriptyline. J Sep Sci 38:1610–1617
29. Wang L, Zhou B, Liu J (2013) Anticancer Polyoxometalates. Prog Chem 25:1131–1141
30. Judd DA, Netlles HJ, Nevis N, Snyder JP, Liotta DC, Tang J, Ermolieff JJ, Schinazi FR, Hill CL (2001) Polyoxometalate HIV-1 protease inhibitors. A new mode of proteas inhibition. J Am Chem Soc 123:886–897
31. Wang X, Liu J, Li J, Liu J (2001) Synthesis, characterization and in vitro antitumor activity of diorganometallo complexes γ-Keggin anions. Inorg Chem Commun 4:372–374
32. Lin Z, Zhongqun L, Wenjun C, Shaojin C (1996) Removing Cs from nuclear waste liquid by crown ether and heteropoly acid: simulated tests. J Radioanal Nucl Chem 205:49–56
33. Heylen S, Smeekens S, Kirschhock CEA, Parac-Vogt TN, Martens JA (2010) Temperature swing adsorption of NOx over Keggin type heteropolyacids. Energy Environ Sci 3:910–916
34. Lihua B, Qizhuang H, Qiong J, Enbo W (2001) Synthesis, properties and crystal structure of $(Gly)_2H_4SiW_{12}O_{40}.5{\cdot}5H_2O$. J Mol Struct 597:83–91
35. Soled S, Miseo S, McVicker G, Gates WE, Gutierrez A, Paes J (1996) Preparation and catalytic properties of supported heteropolyacid salts. Chem Eng J Biochem Eng J 64:247–254
36. Abolghasemi MM, Hassani S, Rafiee E, Yousefi V (2015) Nanoscale-supported heteropoly acid as a new fiber coating for solid-phase microextraction coupled with gas chromatography-mass spectrometry. J Chromatogr A 1381:48–53
37. Chen F, Ma J, Dong Z, Liu R (2014) Characterization and catalytic performance of heteropoly acid $H_4SiW_{12}O_{40}$ supported on nanoporous materials. J Nanosci Nanotechnol 14:7293–7299
38. Badday AS, Abdullah AZ, Lee KT (2014) Transesterification of crude Jatropha oil by activated carbon-supported heteropolyacid catalyst in an ultrasound-assisted reactor system. Renewable Energy 62:10–17
39. Taylor DB, McMonagle JB, Moffat JB (1985) Cation effects on the surface and bulk structure of the salts of 12-tungstosilicic acid. J Colloid Interface Sci 108:278–284
40. Nabizadeh R, Jahangiri Rad R (2016) Nitrate adsorption by pan-oxime-nano Fe_2O_3 using a two-level full factorial design. Res J Nanosci Nanotechnol 6:1–7
41. Jiao H, Wang J (2013) Single crystal ellipsoidal and spherical particles of a-Fe_2O_3: hydrothermal synthesis, formation mechanism, and magnetic properties. J Alloys Compd 577:402–408
42. North EO, Bailar JC, Jonelis FG (2007) Silicotungstic Acid. Inorg Synth 1:129–132
43. Bamoharram FF (2009) Vibrational spectra study of the interactions between Keggin heteropolyanions and amino acids. Molecules 14:3214–3221
44. Kozhevnikov IV, Sinnema A, Jansen RJJ, Bekkum HV (1994) ^{17}O NMR determination of proton sites in solid heteropoly acid $H_3PW_{12}O_{40}$. ^{31}P, ^{29}Si and ^{17}O NMR, FT-IR and XRD study of $H_3PW_{12}O_{40}$ and $H_4SiW_{12}O_{40}$ supported on carbon. Catal Lett 27:187–197
45. Zhao D, Sheng G, Chen C, Wang X (2012) Enhanced photocatalytic degradation of methylene blue under visible irradiation on graphene@TiO_2 dyade structure. Appl Catal B 111:303–308
46. Zhang S, Li J, Zeng M, Zhao G, Xu J, Hu W, Wang X (2013) In situ synthesis of water-soluble magnetic graphitic carbon

nitride photocatalyst and its synergistic catalytic performance. Appl Mater Interfaces 5:12735–12743
47. Yao K, Basnet P, Sessions H, Larsen GK, Hunyadi Murph SE, Zhao Y (2016) Fe_2O_3–TiO_2 core–shell nanorod arrays for visible light photocatalytic applications. Catal Today 270:51–58
48. Zhang S, Fan Q, Gao H, Huang Y, Liu X, Li J, Xu X, Wang X (2016) Formation of Fe_3O_4@MnO_2 ball-in-ball hollow spheres as a high performance catalyst with enhanced catalytic performances. J Mater Chem A 4:1414–1422
49. Guo S, Zhang G (2016) Green synthesis of a bifunctional Fe–montmorillonite composite during the Fenton degradation process and its enhanced adsorption and heterogeneous photo-Fenton catalytic properties. RSC Adv 6:2537–2545
50. Mehraj O, Pirzada BM, Mir NA, Khan MZ, Sabir S (2016) A highly efficient visible-light-driven novel p-n junction Fe_2O_3/BiOI photocatalyst: surface decoration of BiOI nanosheets with Fe_2O_3 nanoparticles. Appl Surf Sci 387:642–651